



**HAL**  
open science

## Design of platinum nanoflower catalyst exhibiting near-ideal local coordination in a complex shape

Alvin Ly, Tristan Asset, Eamonn Murphy, Kaustubh Khedekar, Ying Huang, Li Xing, Mingjie Xu, Hanson Wang, Raphaël Chattot, Xiaoqing Pan, et al.

► **To cite this version:**

Alvin Ly, Tristan Asset, Eamonn Murphy, Kaustubh Khedekar, Ying Huang, et al.. Design of platinum nanoflower catalyst exhibiting near-ideal local coordination in a complex shape. *Electrochimica Acta*, 2023, 469, pp.143282. 10.1016/j.electacta.2023.143282 . hal-04296408

**HAL Id: hal-04296408**

**<https://hal.science/hal-04296408>**

Submitted on 20 Nov 2023

**HAL** is a multi-disciplinary open access archive for the deposit and dissemination of scientific research documents, whether they are published or not. The documents may come from teaching and research institutions in France or abroad, or from public or private research centers.

L'archive ouverte pluridisciplinaire **HAL**, est destinée au dépôt et à la diffusion de documents scientifiques de niveau recherche, publiés ou non, émanant des établissements d'enseignement et de recherche français ou étrangers, des laboratoires publics ou privés.

# Design of Platinum Nanoflower Catalyst Exhibiting Near-ideal Local Coordination in a Complex Shape

Alvin Ly<sup>1,3</sup>, Tristan Asset<sup>1,3,5,\*</sup>, Eamonn Murphy<sup>2</sup>, Kaustubh Khedekar<sup>1,3</sup>, Ying Huang<sup>1,3</sup>, Li Xing<sup>4</sup>, Mingjie Xu<sup>4</sup>, Hanson Wang<sup>1,3</sup>, Raphaël Chattot<sup>6</sup>, Xiaoqing Pan<sup>1,4</sup>, Iryna V. Zenyuk<sup>1,2,3</sup>,  
and Plamen Atanassov<sup>1,2,3,\*</sup>

<sup>1</sup>Department of Materials Science and Engineering, University of California, Irvine

<sup>2</sup>Department of Chemical and Biomolecular Engineering, University of California, Irvine

<sup>3</sup>Advanced Power and Energy Program (APEP), National Fuel Cell Research Center (NFCRC), University of California, Irvine

<sup>4</sup>Irvine Materials Research Institute (IMRI), University of California, Irvine

<sup>5</sup>Institute of Chemistry and Processes for Energy, Environment and Health (ICPEES), UMR 7515 CNRS-Université de Strasbourg, 25 rue Becquerel, 67087 Strasbourg Cedex 02, France

<sup>6</sup>ICGM, Univ. Montpellier, CNRS, ENSCM, Montpellier, France

\*Corresponding Authors.

[t.asset@unistra.fr](mailto:t.asset@unistra.fr)

[plamen.atanassov@uci.edu](mailto:plamen.atanassov@uci.edu)

**Abstract:** Here, we investigate the oxygen reduction reaction activity of near-monocrystalline platinum nanoflowers presenting a low microstrain to decorrelate the contribution of (i) distorted lattice and (ii) high coordination active sites found within the platinum nanoflower pores to the specific activity enhancement. The results are discussed within the framework of previous investigations onto various catalytic nanostructures. We evidenced that the microstrain of the platinum

nanoflowers stands out of the trends previously established for defective platinum-based nanostructures, where the activity is driven by lattice distortion. This indicates that (i) ‘defective’ structures with low lattice distortion, but high variation in coordination number, can be synthesized and (ii) that their specific activity improvement is comparable to the surface distortion approach in liquid electrolyte.

**Keywords:** Oxygen Reduction Reaction; Platinum Nanoflowers; Fuel Cells; Microstrain; Local Coordination

## 1. Introduction

Platinum (Pt) is the leading electrocatalyst for use in hydrogen-based polymer electrolyte membrane fuel cells (PEMFCs) for the sluggish, cathodic oxygen reduction reaction (ORR).<sup>1-7</sup> The scarcity and high price of platinum remain a major roadblock and even state-of-the-art Pt-based catalysts still lack the activity and stability needed for wide-scale commercial deployment.<sup>8,9</sup> To overcome these issues, the recent developments of platinum-based catalysts has turned away from the traditionally small, spherical nanoparticles of platinum to advanced structured nanoparticles in order to improve the intrinsic activity, electrochemically active surface area (ECSA), and stability during operation.<sup>10-12</sup> Starting from the work of Stamenkovic *et al.* that underlined the substantially increased activity of Pt<sub>3</sub>Ni(111) crystal facets and the works from Zhang’s group and Strasser’s group that evidenced the superior performances of Pt<sub>x</sub>Ni octahedral nanoparticles (*i.e.* dominated by (111) facets) for the oxygen reduction reaction,<sup>13-18</sup> new directions have been undertaken to improve platinum-based electrocatalysts activity. Firstly, it was evidenced that the addition of alloying elements to the platinum crystal structure led to higher activities due to the strain effect, *i.e.*

the contraction of the surface lattice parameter by sub-surface 3d-transition metals.<sup>14,19–21</sup> Highly porous structures were also considered of interest due to their high surface area to volume ratio in comparison to their similarly sized solid counterpart, thus significantly increasing the active site density (and ECSA), as well as reducing the amount of precious metal required.<sup>22–24</sup> Finally, structural disorder (*i.e.* variations in the local coordination and lattice parameter) has been shown to greatly influence the ORR performance of platinum-based nanostructures.<sup>12,25,26</sup> In light of the recent progress in electrocatalyst design, two approaches seem to exist, *i.e.* disorder based, which consists of increasing the structural defects density to an optimum and order-based, which evolve around finely tuning the structure to expose the facets with the highest activity, and density of transition metal elements in the sub-surface layers. Within the disorder-based approaches, it can be argued that the contribution of structural defects arises from two different aspects: (i) the variation of the local coordination induced by the presence of crevasses or ad-atoms leading to an over, under or adequate coordination (generalized coordination number below, above or equal to 8.3, respectively) and (ii) the variation of the local lattice parameter, evidenced by the presence of microstrain, leading to either over, under or adequately packed atoms.<sup>27,28</sup> Decorrelating those two contributions is challenging, as structurally disordered electrocatalysts often present both high local variations in the coordination number (*i.e.* high density of crevasses, pores, adatoms) and highly polycrystalline structures that result in important microstrain. The objective of this work is thus to design a nanostructure exhibiting only one kind of structural defect, *i.e.* high variation of the local coordination number (*e.g.* due to porosities) without microstrain (*i.e.* a near monocrystalline structure, without alloying elements) to be compared, performance-wise and physicochemical-wise, with a well-defined and understood defective nanostructure, the platinum-based ‘sea-sponges’<sup>26</sup>. The paper will first discuss the synthetic pathway undergone to achieve said

nanostructure, along with the innovative approach taken to remove active-site-poisoning organics tightly adsorbed or bound to the surface,<sup>29–31</sup> before addressing its ORR activity and how it fits within the family of disordered nanostructures, to finally discussing the implementation of such complex nanostructures in proton exchange membrane fuel cells (PEMFCs).

## **2. Experimental**

### ***2.1. Materials***

Hexachloroplatinic acid (>99.9%), potassium iodide (99%), polyvinylpyrrolidone (40,000 mol wt.), ethylene glycol (99.8%), perchloric acid (70%) were all purchased from Sigma-Aldrich (Milwaukee, Wisconsin, United States of America) and used as-received. Vulcan XC-72R carbon black powder was acquired from Cabot Corporation (Boston, Massachusetts, United States of America) and used as-received. The reference electrocatalyst was acquired and used as-received from TKK (40 wt. % Pt/XC72).

### ***2.2. Platinum Nanoflowers Synthesis***

The synthesis method is a modified polyol method (heating of precursors in a typically diol-based solvent) adapted from a combination of different references, highlighting the effects of potassium iodide in nanostructure formation, such as platinum nanoflowers and PtCu octahedra.<sup>32–34</sup> An amount of PtCl<sub>4</sub> (or H<sub>2</sub>PtCl<sub>6</sub> \* 6(H<sub>2</sub>O)), KI, and polyvinylpyrrolidone (PVP) (in a molar ratio of 1:6 for Pt:I and excess PVP) is mixed in ethylene glycol and heated in a microwave reactor to 180°C. Upon cooling, the nanoparticles are separated by centrifugation and washed with ethanol and hexanes. Then the nanoparticles are redispersed in a water/ethylene glycol mixture where the carbon (Vulcan XC72R) is added for nanoparticle deposition. After 24 hours of mixing, the slurry is vacuum filtered and dried in an oven at 60°C before being ground into a fine powder.

### 2.3. Materials Characterization

X-ray Diffraction (XRD) was performed on a Rigaku Ultima III. A small amount of sample was spread thin and flat over a zero-background silicon holder and the data was collected from  $5^\circ$  to  $90^\circ$  with a scan speed of  $2^\circ/\text{min}$ . Transmission Electron Microscopy (TEM) was performed on a JEOL JEM-2100F. High Resolution Scanning Transmission Electron Microscopy (HR-STEM) and Energy Dispersive X-ray spectroscopy (EDS) was performed on a JEOL JEM-ARM300F. The samples for both methods were the same and prepared by drop casting a small amount of sample in isopropyl alcohol onto a copper grid (300 mesh). Electron Tomography (ET) was done using a JEOL JEM-ARM300F in STEM mode with the same samples used for TEM and STEM imaging and were rotated from  $-20^\circ$  to  $+20^\circ$  in  $1^\circ$  increments. The images were then processed, the tomogram was reconstructed, and the sample rotation video was created using ImageJ, eTomo, and iMovie programs. The electron diffraction-based orientation mapping was collected using the Nanomegas ASTAR on a JEOL JEM-2800. Thermogravimetric Analysis (TGA) was done on a Netzsch TG 209 F1 Libra by heating a small amount of sample powder ( $\sim 2\text{-}10$  mg) in an alumina crucible to  $1100^\circ\text{C}$ . Scanning Electron Microscopy (SEM) was performed on a FEI Magellan 400 XHR. The sample was prepared by dusting a light coating of the sample powder over double sided copper tape mounted on a stub. X-ray Absorption Spectroscopy (XAS) data was collected at the 10-BM beamline of the Advanced Photon Source (APS) at Argonne National Laboratory (ANL). The sample was mixed with binder and pressed as a pellet. The pellet was then sealed in a holder with Kapton tape. Measurements were conducted at the Pt  $L_3$  edge (11.564 keV) in transmission mode. The data was processed and modeled using the Demeter XAS software package.<sup>35</sup> The EXAFS amplitude reduction factor  $S_{02}$  was determined to 0.74 based on the fitting of a standard reference material. The fits were performed in  $k\text{-weight} = 1,2,3$  with a Fourier Transform range of  $3 \text{ \AA}^{-1} \leq k \leq 11.5 \text{ \AA}^{-1}$  ( $dk = 1 \text{ \AA}^{-1}$ ) and fitting window  $1.3 \text{ \AA} \leq R \leq 3.3 \text{ \AA}$ . X-ray Photoelectron Spectroscopy (XPS) was performed on a Kratos AXIS Supra spectrometer with a monochromatic

Al K $\alpha$  source. CasaXPS software was used to analyze the data. Atomic concentrations of different elements were calculated based on their intensities and relative sensitivity factors. The fitting was based on our previous calculations and publications.<sup>36-38</sup> The Wide-Angle X-ray Scattering (WAXS) pattern was measured at the ID31 beamline of the ESRF. The powder sample was loaded in a 1 mm Kapton capillary, and the energy of the X-ray radiations was 75 keV. The scattered signal was collected using a Dectris Pilatus CdTe 2M detector positioned 106 mm behind the sample. Rietveld refinement was performed to extract the crystallite size, lattice and microstrain parameters from the Fm-3m cubic structure of platinum metal using the Fullprof software. The instrumental resolution function was determined by the refinement of a CeO<sub>2</sub> standard sample. The Thomson-Cox-Hastings profile function was adopted. The background of pattern was described by an interpolated set of points with refinable intensities.

#### ***2.4. Electrochemical Characterization***

The electrochemical performance of the catalyst was tested by rotating disc electrode (RDE) with 40  $\mu\text{g}_{\text{Pt}}/\text{cm}^2$  loading on the working electrode (WE) surface (0.247  $\text{cm}^2$ ) and 0.1 M HClO<sub>4</sub> as the electrolyte. The counter electrode (CE) used was a carbon rod and the reference electrode used was a reference hydrogen electrode (RHE). Pure carbon monoxide (99.5%) was introduced by light bubbling in the electrolyte for 5 minutes and then nitrogen gas (99.9999%) was purged through the electrolyte for an extra 25 minutes to remove all excess CO. The working electrode was held at 0.1 V *vs.* RHE (all following potentials are provided *vs.* RHE) during the CO introduction process. The CO stripping cyclic voltammograms were taken at 20 mV/s from 0.1 to 1.2 V for three total cycles. This entire process was then repeated two times. Upon completion of the CO cleaning protocol, the electrochemical cell was washed and the electrolyte refreshed. Pure nitrogen gas (99.9999%) was bubbled in the electrolyte to de-aerate the electrolyte. Then electrochemical impedance spectroscopy (EIS) was done to obtain the uncompensated resistance value for ohmic corrections. 100 activation cycles were done with cyclic voltammetry from 0.1 to 1.2 V at 500 mV/s to clean the

catalyst surface. Then, three cycles of cyclic voltammetry from 0.1 to 1.2 V at 20 mV/s were recorded. Linear sweep voltammograms were taken from 0.05 to 1.05 V at 5 mV/s in nitrogen-saturated and oxygen-saturated (with 99.5% oxygen gas) electrolyte at 1600 RPM.

The electrocatalyst performance was then assessed in proton exchange membrane fuel cell. The cathode and anode catalyst layers were prepared by tape casting of the catalyst ink onto a 50  $\mu\text{m}$  thick PTFE substrate with a wet film thicknesses ranging from 100 – 400  $\mu\text{m}$ . The catalyst ink was prepared to achieve a  $45 \text{ mg}_{\text{carbon}}/\text{mL}_{\text{solvent}}$  with an ionomer to carbon ratio of 0.8. An optimum solvent ratio of 1:1 (DI water: IPA by weight) for a baseline catalyst ink was used while an IPA rich solvent ratio was used for the nanoflower catalyst ink. The ink was roll milled for 18 hours at 60 rpm before tape casting to ensure a homogenous dispersion of the catalyst. A cathode loading of  $0.15 \text{ mg}_{\text{Pt}}/\text{cm}^2$  was targeted while the anode loading was kept at  $0.1 \text{ mg}_{\text{Pt}}/\text{cm}^2$ . The MEAs (5  $\text{cm}^2$  area) were prepared by hot-pressing the anode and cathode catalyst layers (cut out from the tape casted PTFE substrate) onto the Nafion XL membrane and assembled into a Baltic fuel cell testing setup with a 7-channel serpentine flow field. 2% CO gas was introduced to the cathode side and then thoroughly flushed with  $\text{N}_2$  gas before completing the CVs from 0.1 to 1.2 V with a scan rate of 100 mV/s. This process was repeated three times in total. A break-in procedure occurred after the CO treatment with potential holds of 30s at 0.80, 0.60, and 0.30 V each until current density becomes constant. Polarization curves were taken with a 150 kPa back pressure in 100% RH from high to low current densities. EIS was completed from 10 kHz to 0.01 Hz at 0.2 V vs. RHE with 6 pts/decade in a nitrogen-saturated environment on the cathode. Different nanoflower loadings (24 vs. 50 wt. %) were used for liquid and solid characterization, the higher loading allowing for thinner, and therefore more state-of-the-art consistent, catalyst layers (see **Figure S3**). Accelerated Stress Tests (AST) were performed under a  $\text{H}_2$  (anode) /  $\text{N}_2$  (cathode) as square wave cycling between 0.60 V and 0.95 V (3s – 3s) for 30,000 cycles at 80 °C and 100% relative humidity.

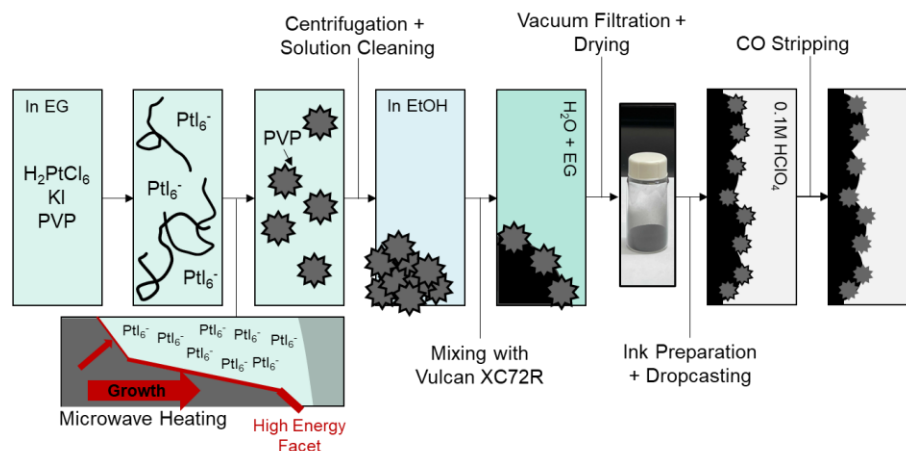


**Figure 1.** Synthesis pathway undergone for the preparation, and cleaning, of the platinum nanoflowers.

### 3. Results and Discussion

#### 3.1. Platinum Nanoflower Synthesis

Hollow and porous nanoparticles have typically been prepared through subtractive growth or etch mechanisms, which tends to produce highly microstrained structures.<sup>23</sup> Here, platinum nanoflowers are synthesized with an adapted polyol method with a suspected additive growth mechanism (**Fig. 1**).<sup>32,39–42</sup> This facile, one-pot synthesis produces a high yield of similar nanostructures with minimal materials synthesis treatments required. The modified polyol synthesis procedure utilizes a platinum salt precursor, iodide ions (for structure formation), and a polymeric surfactant all dispersed in ethylene glycol with microwave-assisted heating.<sup>43–46</sup> Our understanding of the formation mechanism is that the chloride ion complex ( $\text{PtCl}_6^-$ ) shifts in solution to an iodide ion complex ( $\text{PtI}_6^-$ ) with the addition of iodine ions, as indicated by the immediate shift in solution color (yellow  $\rightarrow$  orange  $\rightarrow$  red). Studies of branched platinum nanoparticles have assessed that, if the growth kinetics dominates over the surface diffusion rates, anisotropic growth and anisotropic nanostructures are to be observed as final products.<sup>47</sup> The more stable iodine complex leads to a

higher instantaneous concentration of platinum-based species in solution inducing an easier replenishing of the platinum precursors at the existing platinum seed interface, which thus favor growth limited by kinetics and thus, the growth of higher energy facets.<sup>32</sup>

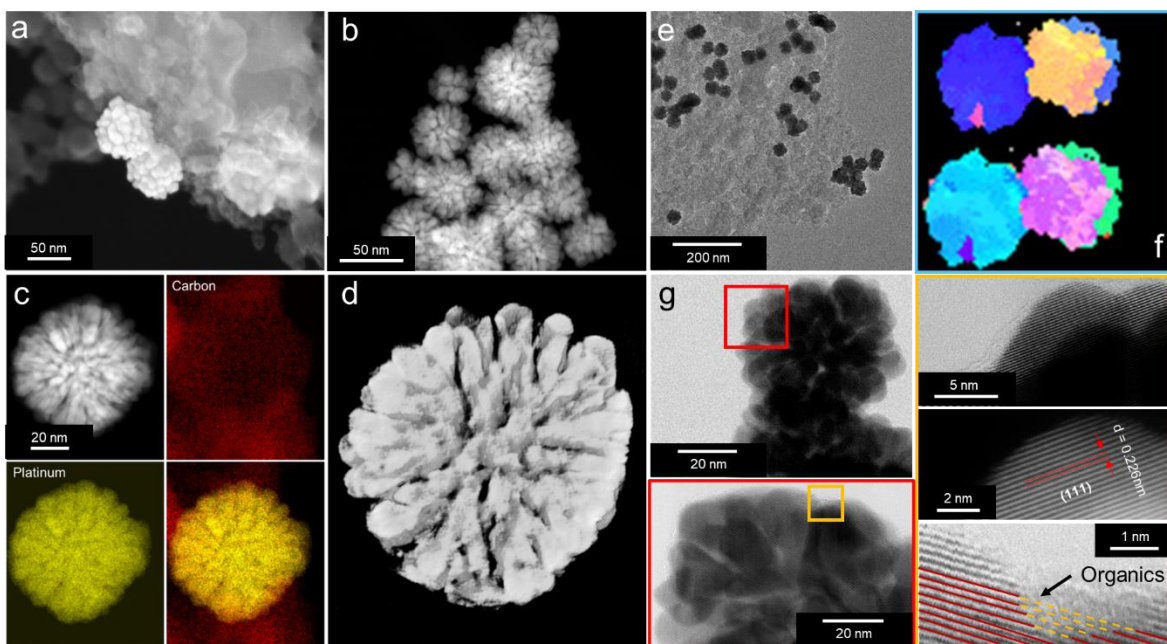


**Figure 2.** Micrographs of the platinum nanoflowers ( $d = 40 - 45$  nm) obtained by (a) SEM, (b) HAADF-STEM on unsupported nanostructures, (c) EDS elemental mapping; (d) electron tomography (see supporting information for the different angles); (e) dispersion of the platinum nanoflowers onto Vulcan XC72R, (f) orientation mapping of the platinum nanoflowers along x and y directions (individual nanoparticle size = *ca.* 45 nm) and (g) high resolution micrographs aiming to provide insights onto (i) the monocrystallinity of the platinum nanoflowers and (ii) the organic presence prior to the CO cleaning step.

### 3.2. Nanoflower Structure

Electron microscopy images show platinum nanoflowers being 40 - 45 nm in size and having good spatial dispersion on the Vulcan XC72R, as illustrated by **Fig. 2**. HR-STEM images show that the

platinum nanoflowers are coated with a 1-2 nm thick layer of organics, as well as display a continuous crystallinity that is unbroken across pore channels (**Fig. 2g**). The crystallite size for these nanoflowers was determined, from the XRD patterns (**Fig. 3**) to be *ca.* 20 nm, which suggests that the structure has a minimal amount of grain boundaries compared to an analogous nanostructure, the “sea-sponge” type platinum-based electrocatalyst.<sup>25</sup> This is further confirmed by (i) the electron diffraction-based orientation mappings (**Fig. 2f**) that evidenced that the nanoflowers are often mono- or bi-crystalline and (ii) the wide angle X-ray scattering, which evidenced a coherent domain size of *ca.* 17.5 nm, thus resulting in a microstrain of 24 %% (percentage of percentage, *i.e.*, divided by 10,000)<sup>26</sup>. For comparison, the “sea-sponges” exhibit a *ca.* 230 %% microstrain for a crystallite size of *ca.* 9 nm. Finally, from synchrotron based X-ray absorption spectroscopy, the XANES and EXAFS data confirm that the nanoflowers behave as reference platinum foil, further confirming the near-monocrystalline nanostructure (**Fig. 3b-c**).<sup>48</sup> Electron tomography of a single nanoflower was completed by a HR-STEM tilt series ( $\pm 20^\circ$ ) and the resulting bright field images were stacked and aligned to create a 3D motion picture of the nanoflower (**Fig. 2d** and supporting video 1). The tomogram was reconstructed using the overlapping data from the tilt series showing the complexity of the inner pore structure, which is continuous from the center of the particle to its surface.

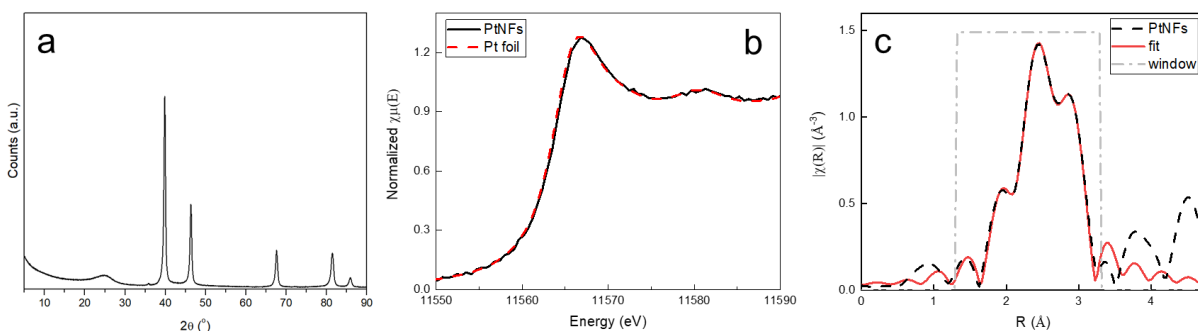


**Figure 3.** Materials properties of the platinum nanoflowers revealed with X-ray characterization: (a) XRD pattern of the nanoflowers supported onto Vulcan XC72R, (b) XANES and (c) EXAFS for the platinum nanoflowers supported on Vulcan XC72R vs. platinum foil (fit).

### ***3.3. Carbon Monoxide Surface Cleaning Protocol***

One of the major issues for the deployment of advanced structured nanoparticles is the remaining adsorbed organics originating from the synthesis process. In this case, polyvinylpyrrolidone (PVP), used as a surfactant, tends to be strongly adsorbed or bound to the surface of the platinum nanoflowers and it is apparent in the HR-STEM images (**Fig. 2g**) and pre-treated electrochemical tests (**Fig. S2**).<sup>30</sup> Bulky organics used in the synthesis are typically removed by either solvent cleaning cycles or heat treatments, however the pore structure of the nanoflowers prevents both methods of removing leftover organics: (i) multiple solution-based cleaning protocols were tested to remove organics, however this type of cleaning had little effect; (ii) high temperature heat treatments (~300-600°C) in inert atmospheres and under vacuum were investigated, however these methods caused significant morphological degradation and complete pore structure collapse of the nanoflowers.<sup>49-51</sup> So, to obtain an electrochemically pristine surface, a carbon monoxide (CO) surface cleaning method was adapted from Gong *et al.*<sup>29</sup>, which allowed the removal of a significant majority of organic molecules from the catalyst surface within three experimental cycles (see experimental section, **Fig. 4** and further confirmation by XPS, see **Fig. S1**, based on the intensity of the N 1s signal). Mechanistically, the CO molecule is (i) able to access the platinum surface in the presence of PVP due to the small molecule size and (ii) strongly bind to the platinum surface, therefore replacing the PVP as the strongly adsorbed surface species and facilitating the removal of PVP through first diffusion/convection and then further during the CO oxidation reaction process (*i.e.*, with CO<sub>2</sub> bubble generation at the reactive interface). Interestingly, the CO cleaning

protocol shows a peak of higher current at higher potential in the first stripping cyclic voltammetry, followed by a much lower current peak shifted to lower potentials in successive strippings, suggesting that the  $\text{CO}_{\text{ads}}$  binding strength is greatly affected by the presence of PVP. This could either arise from (i) the PVP-induced steric obstruction of the platinum surface, which limits accessibility to the  $\text{OH}_{\text{ads}}$  species (needed for CO-oxidation step) or (ii) a PVP-induced modification of the platinum electronic structure, which either strengthens the  $\text{CO}_{\text{ads}}$  adsorption or weakens the  $\text{OH}_{\text{ads}}$  adsorption.<sup>25,26</sup> Notably, the mono-peak signal of the platinum nanoflowers provides further evidence of the near-monocrystallinity of these structures, as Maillard *et al.* evidenced that the presence of grain boundaries was concomitant with the apparition of a pre-peak in the  $\text{CO}_{\text{ads}}$  stripping signal.<sup>52</sup>

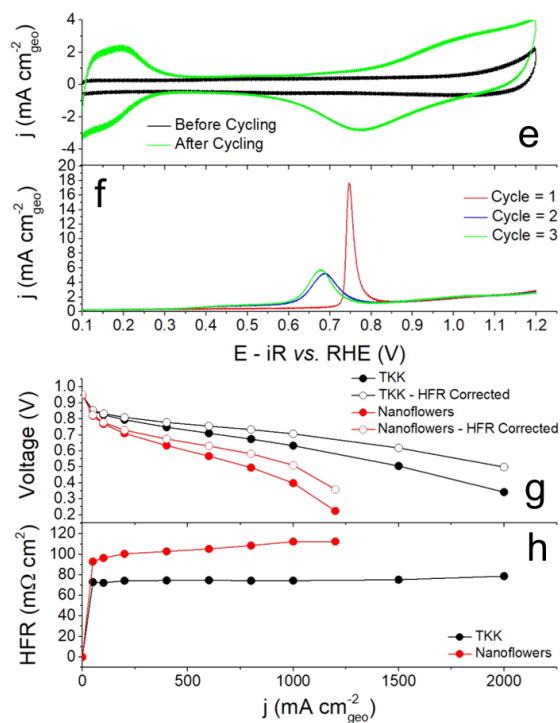
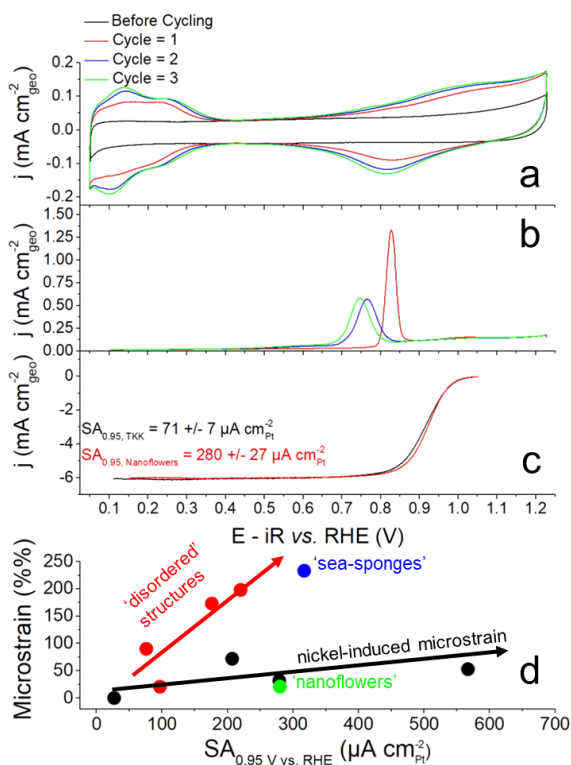


**Figure 4.** Electrochemical properties of the platinum nanoflowers supported on Vulcan XC72R and comparison with the literature: (a) cyclic voltammetry in N<sub>2</sub>-saturated 0.1 M HClO<sub>4</sub> (20 mV s<sup>-1</sup>), before and after CO<sub>ads</sub> cleaning; (b) CO<sub>ads</sub> stripping cycles leading to the surface cleaning; (c) linear sweep voltammetry in O<sub>2</sub>-saturated 0.1 M HClO<sub>4</sub> (20 mV s<sup>-1</sup>, 1600 rpm) for Pt/C provided by TKK and the platinum nanoflowers; (d) microstrain as a function of the specific activity at E vs. RHE = 0.95 V (SA<sub>0.95 V vs. RHE</sub>) for the nanoflowers and the library of electrocatalysts investigated by Chattot *et al.*, *i.e.* ‘ordered’ structures, that exhibit only Ni-induced microstrain; ‘disordered’ structure where the defective nature is dominated by local variation of the lattice parameter, which include the PtNi sea-sponges; (e) cyclic voltammetry during MEA characterization, under N<sub>2</sub>-atmosphere, before and after CO<sub>ads</sub> cleaning; (f) CO<sub>ads</sub> stripping cycles in MEA leading to the surface cleaning; (g – h) polarization curves measured under air, with a backpressure of 150 kPa and 100% relative humidity, for the platinum nanoflowers and the Pt/C TKK reference, along with the variations of the high frequency resistance (HFR) as a function of the current density; (g) also presents the data corrected from the HFR.

### 3.4. Nanoflowers ORR Performance

The catalytic activity of the nanoflowers towards the ORR was studied in 0.1 M HClO<sub>4</sub>. It was found that, like most catalysts having advanced structure, they suffered from a significantly lower ECSA compared to traditional nanoparticle standards (TKK), *i.e.* 12 m<sup>2</sup> g<sub>Pt</sub><sup>-1</sup> (platinum nanoflowers, calculated from the H<sub>upd</sub>) or 13 m<sup>2</sup> g<sub>Pt</sub><sup>-1</sup> (platinum nanoflowers, calculated from the CO<sub>ads</sub> stripping) vs. 90 m<sup>2</sup> g<sub>Pt</sub><sup>-1</sup> (TKK, calculated from the H<sub>upd</sub>). This impacts the nanoflowers activity in the following way: although the nanoflowers present a higher specific activity (280, nanoflowers, vs. 71, TKK, μA cm<sup>-2</sup><sub>Pt</sub> at 0.95 V vs. RHE), the mass activity is lower (45, nanoflowers, vs. 65, TKK, A g<sup>-1</sup><sub>Pt</sub> at 0.95 V vs. RHE), see **Figure 4c**). This nevertheless implies that some of the nanoflowers active sites exhibit far higher intrinsic activity than the Pt/C active sites, as evidenced by the differences in specific activities. Owing to the fact that the nanoflowers do not present

clearly defined facets, by opposition to nanostructures such as  $\text{Pt}_x\text{Ni}$  octahedra, this intrinsic activity enhancement is likely to arise from structural defects and, more specifically, (i) surface lattice distortion or (ii) variations in the local coordination number. Identifying which of these two dominates can be done by comparing these structures to those discussed by Chattot *et al.*<sup>25,26</sup>. Here, we aim to assess if the specific activity *vs.* microstrain of the platinum nanoflowers follow the same trend as observed for nanostructures for which the intrinsic activity results from high lattice distortion. This trend is presented in **Fig. 4d**. The nanoflowers present a low microstrain (21%), which brings them within the family of catalysts where the microstrain solely results from the presence of an alloying element – which, incidentally, is absent from the platinum nanoflowers. This further strengthens the hypothesis that their activity improvement is neither correlated to surface distortion or strain, ligand, or specific orientation effects, but to local variations of the generalized coordination number. It is interesting to consider these findings in the prism of the work by Rück *et al.*, which highlights how the optimal coordination number can be translated in electrocatalysts morphology, such as platinum rods with integrated concavities.<sup>53</sup> There, they highlighted that rods, modified with *ca.* 2 nm diameters concavities could lead in specific activity improvement for the ORR of *ca.* 6 – 8. Such structures share similarities with the platinum nanoflowers, in the sense that the ‘petals’ can be seen as rods, and the porosities in-between as the integrated concavities that host the near-optimal catalytic sites. An argument could be made that the activity improvement mainly arises from the crystallite size of the platinum nanoflowers, through the so-called particle size effect, *i.e.* that the specific activity of a cubooctahedral nanoparticle increases with its size, reaching near-polycrystalline platinum activity at size of 20 nm, which corresponds with a *ca.* 3-4 increase in specific activity *vs.* 3 nm platinum nanoparticles.<sup>54</sup> Keeping in mind that this effect can also be expressed in terms of active site coordination (*i.e.*, by moving from low

coordination active sites in 3 nm nanoparticles to increased coordination number in larger nanoparticles), it is likely that it does not reach the same extent in porous, highly complex structures, where the pseudo-(111) surface is rigged by porosities, but its contribution cannot be excluded altogether. In conclusion, the specific activity improvement for the platinum nanoflowers arises from a higher density of near-optimally coordinated active sites, coming from the inner porosities and the larger crystallite size.

Keeping in mind the final application of the platinum nanoflowers, the catalyst was integrated as cathode catalyst layers into membrane electrode assemblies (MEAs) of PEMFCs. Several critical findings were established: (i) the  $\text{CO}_{\text{ads}}$  stripping cleaning method worked to a certain degree in a solid electrolyte environment, as evidenced in **Fig. 4e-f**, **Fig. S1** and **Fig. S4**; (ii) the performance of the platinum nanoflowers under an air-atmosphere was lower compared to the Pt/C TKK standard (**Fig. 4g**). From the  $\text{H}_{\text{upd}}$  region, the ECSA for platinum nanoflowers supported on carbon was  $7 \text{ m}^2 \text{ g}^{-1}$  (resulting in a loss of ~40%) compared to  $31 \text{ m}^2 \text{ g}^{-1}$  (resulting in a loss of ~66%) for TKK Pt/C. The specific surface losses were expected to be higher for the nanoflowers, due to their porous structure. Hence, we assume that the observed phenomena indicates that part of the ECSA was already non-accessible in the nanoflowers in liquid electrolyte (*e.g.*, within the intricate pore structure), which led to a lower decrease when moving toward an MEA. The open circuit voltage (OCV) was similar between the platinum nanoflowers and Pt/C cathodes, however, within the ohmic region the PEMFCs with nanoflowers showed elevated high-frequency-resistance (HFR) which was close to double that of Pt/C (see **Fig. 4h**). This HFR increase might be induced by the poisoning of the catalytic layer with the organics removed through the CO cleaning procedure,

combined with sub-optimal ionomer content in the catalyst layer, and/or internal contact resistances. Correcting the signal from the HFR did not fully close the gap in performances between the Pt/C TKK standard and the platinum nanoflowers (see **Fig. 4g**), thus indicating that mass transport and kinetic limitations also contribute to this depreciated activity in a solid electrolyte environment. These issues might arise from the losses in ECSA from the liquid to solid environment, indicative of a decreased accessibility to the porous network of the nanoflowers, which are theoretically hosting the closest-to-optimal coordination number active sites (within the concavities of the pores), by the ionomer and the O<sub>2</sub>. This effect is of smaller impact onto the commercial electrocatalyst, owing to the somewhat identical active nature of all active sites on the 2-3 nm nanoparticles and, thus, the fact that no specific type (*e.g.*, highly coordinated) was lost during the liquid-to-solid transition. Finally, the durability of those nanostructures was investigated in PEM-FCs, following a load cycle (0.6 – 0.95 V, 30,000 cycles) protocol, and 44% current losses at 0.6 V were observed for the nanoflowers, *vs.* 65% for the commercial Pt/C (see **Fig. S5**). However, this higher stability comes at the cost of the complete disappearance of the inner porous network observed on the fresh samples, thus removing any beneficial effect induced by the local coordination variations (see **Fig. S6**), that ultimately transform in *ca.* 40 nm non-porous platinum nanoparticles.

#### 4. Conclusions

In summary, we successfully synthesized platinum nanoflowers with intrinsic activity mainly driven by active sites with near-ideal coordination, as they exhibited little microstrain, along with the absence of (i) alloying elements and (ii) extended facets. As such, these nanostructures present an interesting counterpart to the ‘surface distortion’ based nanostructures, evidencing that similar

intrinsic activity can be achieved through the use of different kinds of structural defects. The implementation of those nanostructures in PEMFC remains challenging, as they not only (i) suffer from an increased HFR resistance, indicative from a dire need to carefully rethink the ink formulation for those larger nanostructures, which dispersion onto the carbon surface is widely different from classic, 2-3 nm, platinum nanoparticles, and their cleaning procedure but also (ii) a decreased ECSA and higher mass transport resistance, indicative of a decreased accessibility to the inner porous network of the nanoflowers, which is believed to host some of the most active catalytic sites. We believe that reporting on these lower performances in PEMFC is nonetheless critical, as the implementation of such complex structures in PEMFCs remains little discussed and it highlights the necessity to consider electrocatalysts' design within the prism of their final application and/or to re-adapt said final application to the new generation of electrocatalysts.<sup>7</sup> Previous works<sup>24,55-60</sup> have investigated the specifics of ink formulation development which can have significant impact on the catalyst performance. However, the identified parameters may require significant tailoring based on the catalyst size, structure, and composition. A brief summary of some of the main factors that can affect how the ionomer (typically Nafion<sup>®</sup>) or the proton conductor interface with the catalytic sites include (i) changing the solvent types and ratios as those parameters strongly impact onto the ionomer aggregation and, thus, integration into the porosities, (ii) changing the ionomer structure (*e.g.*, in the main or side chain structures) to facilitate its incorporation into said pores or (iii) introducing a buffer material (*e.g.*, ionic liquids) to connect the catalyst surface to the ionomer. The latter approach was successfully undertaken by Snyder et al. on porous NiPt-based nanoparticles, leading to a 10-fold increase of the specific activity at 0.95 V vs. RHE.<sup>61</sup> Owing the relatively small pores size, and the resulting size-exclusion of the ionomer,

the use of an ionic liquid might appear as the most promising solution to use the full potential of such complex Pt-based nanostructures.

**Acknowledgments:** The authors acknowledge the use of facilities and instrumentation at the UC Irvine Materials Research Institute (IMRI), which is supported in part by the National Science Foundation through the UC Irvine Materials Research Science and Engineering Center (DMR-2011967). XPS work was performed using instrumentation funded in part by the National Science Foundation Major Research Instrumentation Program under grant no. CHE-1338173. MRCAT operations are supported by the Department of Energy and the MRCAT member institutions. This research used resources of the Advanced Photon Source, a U.S. Department of Energy (DOE) Office of Science User Facility operated for the DOE Office of Science by Argonne National Laboratory under Contract No. DE-AC02-06CH11357. RC gratefully acknowledge the ESRF for the provision of beamtime at ID31 beamline as well as financial support from the French National Research Agency through the HOLYCAT project (grant number n° ANR-22-CE05-0007).

**Authors Contributions:** AL: Conceptualization, Methodology, Investigation, Writing - Original Draft, Writing - Review & Editing, Visualization, Formal analysis; TA: Writing - Original Draft, Writing - Review & Editing, Visualization, Formal analysis, Supervision; EM, MX, HW, LX, RC, KK: Investigation, Formal analysis; XP, IVZ, PA: Supervision, Project administration, Funding acquisition. All authors: Writing - Review & Editing.

**Competing Interests:** the authors are declaring no competing interests.

## References

1. Greeley, J. *et al.* Alloys of platinum and early transition metals as oxygen reduction electrocatalysts. *Nature Chemistry* **1**, 552–556 (2009).
2. Li, Y. *et al.* Recent Progresses in Oxygen Reduction Reaction Electrocatalysts for Electrochemical Energy Applications. *Electrochem. Energ. Rev.* **2**, 518–538 (2019).
3. Pan, L., Ott, S., Dionigi, F. & Strasser, P. Current challenges related to the deployment of shape-controlled Pt alloy oxygen reduction reaction nanocatalysts into low Pt-loaded cathode layers of proton exchange membrane fuel cells. *Current Opinion in Electrochemistry* **18**, 61–71 (2019).
4. Fan, J. *et al.* Bridging the gap between highly active oxygen reduction reaction catalysts and effective catalyst layers for proton exchange membrane fuel cells. *Nat Energy* **6**, 475–486 (2021).
5. Moriau, L. J. *et al.* Resolving the nanoparticles' structure-property relationships at the atomic level: a study of Pt-based electrocatalysts. *iScience* **24**, 102102 (2021).
6. Zhang, J. *et al.* Stabilizing Pt-Based Electrocatalysts for Oxygen Reduction Reaction: Fundamental Understanding and Design Strategies. *Advanced Materials* **n/a**, 2006494.
7. Ly, A., Asset, T. & Atanassov, P. Integrating nanostructured Pt-based electrocatalysts in proton exchange membrane fuel cells. *Journal of Power Sources* **478**, 228516 (2020).
8. Xia, W., Mahmood, A., Liang, Z., Zou, R. & Guo, S. Earth-Abundant Nanomaterials for Oxygen Reduction. *Angewandte Chemie International Edition* **55**, 2650–2676 (2016).
9. Asset, T. & Atanassov, P. Iron-Nitrogen-Carbon Catalysts for Proton Exchange Membrane Fuel Cells. *Joule* **4**, 33–44 (2020).
10. Rudi, S., Cui, C., Gan, L. & Strasser, P. Comparative Study of the Electrocatalytically Active Surface Areas (ECSAs) of Pt Alloy Nanoparticles Evaluated by Hupd and CO-stripping voltammetry. 13.
11. Meier, J. C. *et al.* Design criteria for stable Pt/C fuel cell catalysts. *Beilstein J. Nanotechnol.* **5**, 44–67 (2014).

12. Li, M. *et al.* Ultrafine jagged platinum nanowires enable ultrahigh mass activity for the oxygen reduction reaction. *Science* **354**, 1414–1419 (2016).
13. Cui, C. *et al.* Octahedral PtNi Nanoparticle Catalysts: Exceptional Oxygen Reduction Activity by Tuning the Alloy Particle Surface Composition. *Nano Lett.* **12**, 5885–5889 (2012).
14. Stamenkovic, V. R. *et al.* Trends in electrocatalysis on extended and nanoscale Pt-bimetallic alloy surfaces. *Nature Materials* **6**, 241–247 (2007).
15. Stamenkovic, V. R. *et al.* Improved Oxygen Reduction Activity on Pt<sub>3</sub>Ni(111) via Increased Surface Site Availability. *Science* **315**, 493–497 (2007).
16. K. Chaudhari, N. *et al.* Recent advances in electrocatalysts toward the oxygen reduction reaction: the case of PtNi octahedra. *Nanoscale* **10**, 20073–20088 (2018).
17. Li, B. *et al.* High performance octahedral PtNi/C catalysts investigated from rotating disk electrode to membrane electrode assembly. *Nano Res.* **12**, 281–287 (2019).
18. Zhang, J., Yang, H., Fang, J. & Zou, S. Synthesis and Oxygen Reduction Activity of Shape-Controlled Pt<sub>3</sub>Ni Nanopolyhedra. *Nano Lett.* **10**, 638–644 (2010).
19. Lopes, P. P. *et al.* Eliminating dissolution of platinum-based electrocatalysts at the atomic scale. *Nat. Mater.* **19**, 1207–1214 (2020).
20. Wang, C. *et al.* Synthesis of Homogeneous Pt-Bimetallic Nanoparticles as Highly Efficient Electrocatalysts. *ACS Catal.* **1**, 1355–1359 (2011).
21. Tian, X. *et al.* Engineering bunched Pt-Ni alloy nanocages for efficient oxygen reduction in practical fuel cells. *Science* **366**, 850–856 (2019).
22. Snyder, J., McCue, I., Livi, K. & Erlebacher, J. Structure/Processing/Properties Relationships in Nanoporous Nanoparticles As Applied to Catalysis of the Cathodic Oxygen Reduction Reaction. *J. Am. Chem. Soc.* **134**, 8633–8645 (2012).
23. Dubau, L. *et al.* Tuning the Performance and the Stability of Porous Hollow PtNi/C Nanostructures for the Oxygen Reduction Reaction. *ACS Catal.* **5**, 5333–5341 (2015).

24. Chen, C. *et al.* Highly Crystalline Multimetallic Nanoframes with Three-Dimensional Electrocatalytic Surfaces. *Science* **343**, 1339–1343 (2014).
25. Chattot, R. *et al.* Beyond Strain and Ligand Effects: Microstrain-Induced Enhancement of the Oxygen Reduction Reaction Kinetics on Various PtNi/C Nanostructures. *ACS Catal.* **7**, 398–408 (2017).
26. Chattot, R. *et al.* Surface distortion as a unifying concept and descriptor in oxygen reduction reaction electrocatalysis. *Nature Materials* **17**, 827 (2018).
27. Calle-Vallejo, F. *et al.* Finding optimal surface sites on heterogeneous catalysts by counting nearest neighbors. *Science* **350**, 185–189 (2015).
28. Bacq, O. L. *et al.* Effect of Atomic Vacancies on the Structure and the Electrocatalytic Activity of Pt-rich/C Nanoparticles: A Combined Experimental and Density Functional Theory Study. *ChemCatChem* **9**, 2324–2338 (2017).
29. Gong, K., Vukmirovic, M. B., Ma, C., Zhu, Y. & Adzic, R. R. Synthesis and catalytic activity of Pt monolayer on Pd tetrahedral nanocrystals with CO-adsorption-induced removal of surfactants. *Journal of Electroanalytical Chemistry* **662**, 213–218 (2011).
30. Tsuji, M. *et al.* Toward to branched platinum nanoparticles by polyol reduction: A role of poly(vinylpyrrolidone) molecules. *Colloids and Surfaces A: Physicochemical and Engineering Aspects* **317**, 23–31 (2008).
31. Safo, I. A., Dosche, C. & Oezaslan, M. TEM, FTIR and Electrochemistry Study: Desorption of PVP from Pt Nanocubes. *Zeitschrift für Physikalische Chemie* **232**, 1319–1333 (2018).
32. Yin, J., Wang, J., Li, M., Jin, C. & Zhang, T. Iodine Ions Mediated Formation of Monomorphic Single-Crystalline Platinum Nanoflowers. *Chem. Mater.* **24**, 2645–2654 (2012).
33. Yang, J. *et al.* Facile Microwave-Assisted Synthesis of Concave Octahedral Pt–Cu Alloy Nanocrystals and their Electrocatalytic Properties. *ChemNanoMat* **4**, 909–913 (2018).
34. Ly, A., Asset, T., Murphy, E. & Atanassov, P. Platinum Nanoflowers: A New Class of Nanostructured Electrocatalysts for the Oxygen Reduction Reaction. *Meet. Abstr.* **MA2021-02**, 1278 (2021).

35. Ravel, B. & Newville, M. ATHENA, ARTEMIS, HEPHAESTUS: data analysis for X-ray absorption spectroscopy using IFEFFIT. *J Synchrotron Rad* **12**, 537–541 (2005).
36. Patel, A. *et al.* Investigating the effects of proton exchange membrane fuel cell conditions on carbon supported platinum electrocatalyst composition and performance. *Journal of Vacuum Science & Technology A* **30**, 04D107 (2012).
37. Khedekar, K. *et al.* Probing Heterogeneous Degradation of Catalyst in PEM Fuel Cells under Realistic Automotive Conditions with Multi-Modal Techniques. *Advanced Energy Materials* **11**, 2101794 (2021).
38. Jia, Q., Lewis, E. A., Grice, C., Smotkin, E. S. & Segre, C. U. In situ XAFS studies of the oxygen reduction reaction on carbon supported Pt and PtNi(1:1) catalysts. *J. Phys.: Conf. Ser.* **190**, 012157 (2009).
39. Li, J. *et al.* Synthesis of Platinum Nanocrystals within Iodine Ions Mediated. *Journal of Nanomaterials* <https://www.hindawi.com/journals/jnm/2018/1465760/> (2018) doi:10.1155/2018/1465760.
40. Asset, T. *et al.* Activity and Durability of Platinum-Based Electrocatalysts Supported on Bare or Fluorinated Nanostructured Carbon Substrates. *J. Electrochem. Soc.* **165**, F3346–F3358 (2018).
41. Oh, H.-S., Oh, J.-G., Hong, Y.-G. & Kim, H. Investigation of carbon-supported Pt nanocatalyst preparation by the polyol process for fuel cell applications. *Electrochimica Acta* **52**, 7278–7285 (2007).
42. Oh, H.-S., Oh, J.-G. & Kim, H. Modification of polyol process for synthesis of highly platinum loaded platinum–carbon catalysts for fuel cells. *Journal of Power Sources* **183**, 600–603 (2008).
43. Tabatabaei, K. *et al.* Halogen-Induced Crystallinity and Size Tuning of Microwave Synthesized Germanium Nanocrystals. *Chem. Mater.* **31**, 7510–7521 (2019).
44. Xiang Chen, W., Yang Lee, J. & Liu, Z. Microwave-assisted synthesis of carbon supported Pt nanoparticles for fuel cell applications. *Chemical Communications* **0**, 2588–2589 (2002).
45. Harada, M. & Cong, C. Microwave-Assisted Polyol Synthesis of Polymer-Protected Monometallic Nanoparticles Prepared in Batch and Continuous-Flow Processing. *Ind. Eng. Chem. Res.* **55**, 5634–5643 (2016).

46. Kundu, P. *et al.* Ultrafast Microwave-Assisted Route to Surfactant-Free Ultrafine Pt Nanoparticles on Graphene: Synergistic Co-reduction Mechanism and High Catalytic Activity. *Chem. Mater.* **23**, 2772–2780 (2011).
47. Cheong, S., Watt, J., Ingham, B., Toney, M. F. & Tilley, R. D. In Situ and Ex Situ Studies of Platinum Nanocrystals: Growth and Evolution in Solution. *J. Am. Chem. Soc.* **131**, 14590–14595 (2009).
48. Marinkovic, N., Sasaki, K. & Adzic, R. Nanoparticle size evaluation of catalysts by EXAFS: Advantages and limitations. *Zas Mat* **57**, 101–109 (2016).
49. Long, N. V., Ohtaki, M., Nogami, M. & Hien, T. D. Effects of heat treatment and poly(vinylpyrrolidone) (PVP) polymer on electrocatalytic activity of polyhedral Pt nanoparticles towards their methanol oxidation. *Colloid Polym Sci* **289**, 1373–1386 (2011).
50. Cai, X., Lin, R., Liu, X. & Zhao, Y. Effect of heat treatment on the surface structure of Pd@Pt–Ni core-shell catalysts for the oxygen reduction reaction. *Journal of Alloys and Compounds* **884**, 161059 (2021).
51. Bezerra, C. W. B. *et al.* A review of heat-treatment effects on activity and stability of PEM fuel cell catalysts for oxygen reduction reaction. *Journal of Power Sources* **173**, 891–908 (2007).
52. Maillard, F. *et al.* Influence of particle agglomeration on the catalytic activity of carbon-supported Pt nanoparticles in CO monolayer oxidation. *Phys. Chem. Chem. Phys.* **7**, 385–393 (2005).
53. Rück, M., Bandarenka, A., Calle-Vallejo, F. & Gagliardi, A. Fast identification of optimal pure platinum nanoparticle shapes and sizes for efficient oxygen electroreduction. *Nanoscale Adv.* **1**, 2901–2909 (2019).
54. Shinozaki, K., Morimoto, Y., Pivovar, B. S. & Kocha, S. S. Re-examination of the Pt Particle Size Effect on the Oxygen Reduction Reaction for Ultrathin Uniform Pt/C Catalyst Layers without Influence from Nafion. *Electrochimica Acta* **213**, 783–790 (2016).
55. Uchida, M., Aoyama, Y., Eda, N. & Ohta, A. New Preparation Method for Polymer-Electrolyte Fuel Cells. *J. Electrochem. Soc.* **142**, 463 (1995).

56. Uchida, M., Aoyama, Y., Eda, N. & Ohta, A. Investigation of the Microstructure in the Catalyst Layer and Effects of Both Perfluorosulfonate Ionomer and PTFE-Loaded Carbon on the Catalyst Layer of Polymer Electrolyte Fuel Cells. *J. Electrochem. Soc.* **142**, 4143 (1995).
57. Ngo, T. T., Yu, T. L. & Lin, H.-L. Influence of the composition of isopropyl alcohol/water mixture solvents in catalyst ink solutions on proton exchange membrane fuel cell performance. *Journal of Power Sources* **225**, 293–303 (2013).
58. Ngo, T. T., Yu, T. L. & Lin, H.-L. Nafion-based membrane electrode assemblies prepared from catalyst inks containing alcohol/water solvent mixtures. *Journal of Power Sources* **238**, 1–10 (2013).
59. Ott, S. *et al.* Ionomer distribution control in porous carbon-supported catalyst layers for high-power and low Pt-loaded proton exchange membrane fuel cells. *Nature Materials* **19**, 77–85 (2020).
60. Chao, L. *et al.* Impact of Catalyst Ink Dispersing Solvent on PEM Fuel Cell Performance and Durability. *J. Electrochem. Soc.* (2021) doi:10.1149/1945-7111/abf2b0.
61. Snyder, J., Livi, K. & Erlebacher, J. Oxygen Reduction Reaction Performance of [MTBD][beti]-Encapsulated Nanoporous NiPt Alloy Nanoparticles. *Advanced Functional Materials* **23**, 5494–5501 (2013).